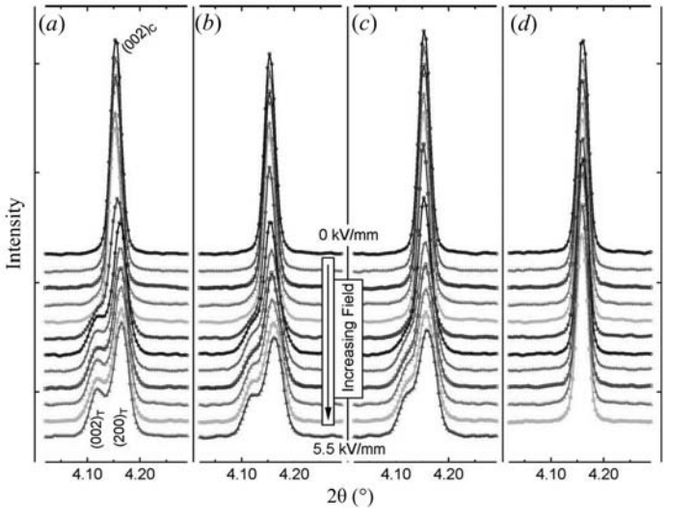

Figure 2.8.10
The pseudo-cubic 002 reflection of (*a*) 0.93BNT–0.07BT end member, (*b*) 0.938BNT–0.053BT–0.009KNN, (*c*) 0.932BNT–0.045BT–0.023KNN and (*d*) 0.86BNT–0.14KNN end member as a function of electric field from the initial zero-field state (top) to an applied field of 5.5 kV mm^{-1} (bottom). The sample orientation is such that the scattering vector is parallel to the electric field. Reproduced with permission from Daniels *et al.* (2010). Copyright (2010) Elsevier.

above a threshold of 0.5 kV mm^{-1}, a very pronounced distortion is observed for 0.93BNT–0.07BT, which eventually above 2 kV mm^{-1} develops into a tetragonal structure. In addition to the combination of various compositions, the authors simultaneously measured the X-ray fluorescence spectra, thus confirming the actual composition.

Fig. 2.8.11 depicts a Rietveld refinement of a lead-free ferroelectric material with the composition $0.92Ba_{0.5}Na_{0.5}TiO_3$–$0.06BaTiO_3$–$0.02K_{0.5}Na_{0.5}NbO_3$. New superstructure reflections (Fig. 2.8.11*b*, arrows) and a lattice distortion (Fig. 2.8.11*b*, circled) were observed due to a transition from space group *P*4*bm* to *R*3*c* (Hinterstein *et al.*, 2010).

In an overview, Jones summarized the use of diffraction techniques. Along with the importance of microdiffraction, diffuse scattering and texture effects, the importance of time-resolved studies including stroboscopy was acknowledged (Jones, 2007).

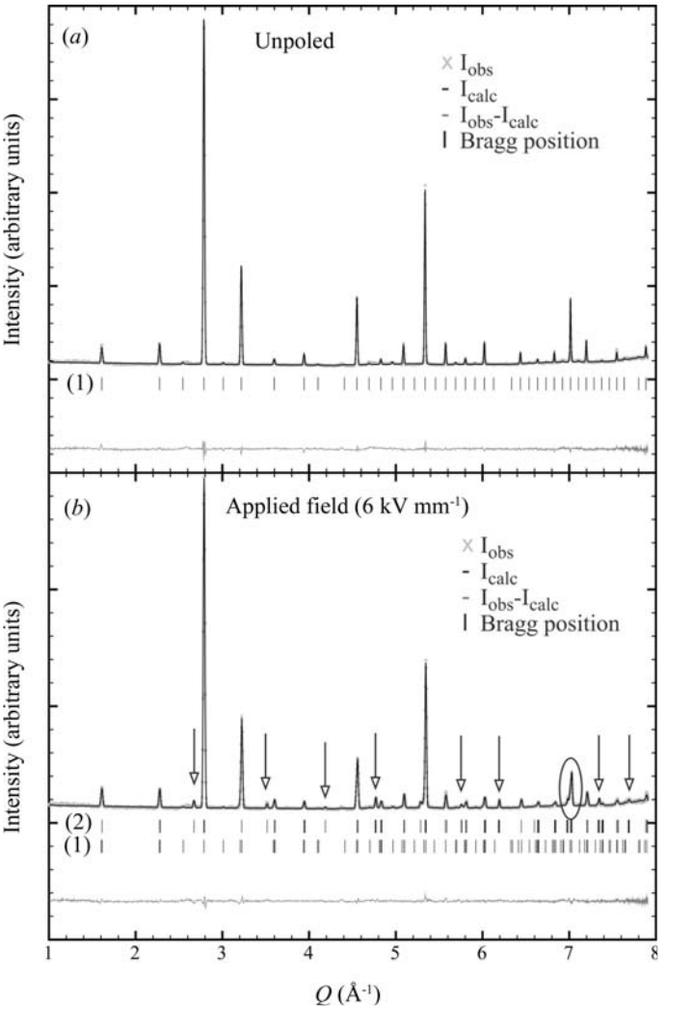

Figure 2.8.11
Rietveld refinement based on different patterns of $0.92Bi_{0.5}Na_{0.5}TiO_3$–$0.06BaTiO_3$–$0.02K_{0.5}NbO_3$ (*a*) in the unpoled and (*b*) in the applied field state at 6 kV mm^{-1}. Experimental data are shown by grey crosses, black lines denote calculated profiles, and the lower plot shows their difference. Calculated positions of Bragg reflections are shown by vertical tick marks, where the different rows correspond to the initial tetragonal phase with space group *P*4*bm* (1) and the field-induced rhombohedral phase with space group *R*3*c* (2). Arrows mark superlattice reflections of type $\frac{1}{2}\{ooe\}$ and the circle highlights the rhombohedral split 331_C reflection.

2.8.3.2. *In situ studies of electrode materials and in operando investigations of Li-ion batteries*

Rechargeable energy sources in mobile electronics are mainly based on lithium-ion batteries. Their application relies on the mobility of the small Li ions, which move from the cathode through an electrolyte to the anode during charge and back during discharge. Intensive research is underway to improve the performance of such energy-storage technology. High gravimetric and volumetric energy and power densities are required. Other additional challenges are safety, lifetime, the temperature range of stable operation and production costs per unit energy at the battery level. Knowledge of the correlation between the electrochemical functionality and the structure of the electrode materials during Li exchange is essential in order to interpret the underlying mechanisms and degradation processes and to find a promising approach to better materials. The high reactivity of the cell components and the very strong interactions between materials inside an electrochemical cell require studies on complete operational devices by non-invasive *in operando* methods. So-called electrochemical 'half cells' are often studied to follow structural changes in electrode materials. These are complete operational cells, but the electrode is cycled against an Li-metal counter electrode. Such half-cell studies are sometimes described as *in situ* studies. Limitations might occur with respect to fatigue studies and at very high charge and discharge rates, when the performance is determined by the Li-metal electrode. The classification of *in situ* and *in operando* methods is not unambiguous in structural studies on battery materials. Sometimes the term *quasi in situ* is used for studies where specific states of the materials are prepared electrochemically and handled in an Ar atmosphere with complete protection against humidity and air, but actually investigated *ex situ* (Oswald *et al.*, 2009).

Some early *in situ* setups have been described for neutron diffraction (Bergstöm, Andersson *et al.*, 1998) and transmission X-ray diffraction (Bergström, Gustafsson & Thomas, 1998), and also at elevated temperatures (Eriksson *et al.*, 2001). Today, for example, good-quality full diffraction patterns can be obtained

Copyright © 2018 International Union of Crystallography

with exposure times well below 100 ms using synchrotron radiation (Herklotz *et al.*, 2013). Capillary-based micro-battery cells allow for *in situ* X-ray powder diffraction studies on one single electrode (Johnsen & Norby, 2013). Even spatially resolved neutron diffraction studies are possible on commercial cylindrical Li-ion batteries (Senyshyn *et al.*, 2015).

The mechanism of Li extraction and insertion differs for different types of electrodes. In intercalation-type electrodes the topology of the host structure remains mainly unchanged, and suitable sites in the structure are either occupied by Li or are vacant in the delithiated state. This use of intercalation chemistry for electrochemical energy storage was established for a battery based on Li metal as the negative electrode and TiS_2 as the positive electrode (Whittingham, 1976). In commercial cells today the negative electrode is also based on intercalation and consists of layered graphite, which hosts Li during the charge cycle up to the composition LiC_6. Another working mechanism for negative electrodes is electrochemical alloying with Li. The most promising examples involve Si, Al and Sn. These electrode concepts suffer from extreme volume changes: 100% for Al $\rightarrow$ LiAl or even 300% for Si $\rightarrow$ $Li_{21}Si_5$. In combination with the brittleness of these materials, the particles break down and become amorphous during successive charging and discharging, accompanied by contact losses and resulting pronounced fade in capacity. Two other mechanisms have also received considerable attention as they allow higher specific capacities. In a replacement reaction, one transition metal is replaced by Li while the topology of the structure is mainly preserved. During a conversion or displacement reaction the initial structures of transition-metal compounds, for example nanometre-sized oxides (Poizot *et al.*, 2000) or other binary compounds (Cabana *et al.*, 2010), are believed to be destroyed completely by either amorphization or phase transitions. The transition-metal ions are reduced to metallic nanoparticles, which are embedded in a complex network of Li_2O and reaction products from the electrolyte. In spite of the loss of long-range order, an important short-range structure remains. This has been shown in detail for ternary Cu–Fe oxides (Adam *et al.*, 2013). The reduction of Cu^{2+} from CuO takes place through the formation of a Cu_2O/Li_2O composite, in which Cu_2O reacts further to form Cu metal and Li_2O. Spinel-type $CuFe_2O_4$ and $CuFeO_2$ react to form α-$LiFeO_2$ with the extrusion of metallic Cu and Fe nanoparticles. At even lower potentials against Li^+/Li between 0.8 and 1.0 V, α-$LiFeO_2$ is further reduced into metallic Fe nanoparticles and Li_2O. While most of these displacement reactions suffer from very poor reversibility, good cycling stability was shown for $Cu_{2.33}V_4O_{11}$ (Morcrette *et al.*, 2003). During cell discharge Li penetrates into the well crystallized copper vanadate, forming a solid solution up to an Li content of $x = 0.6$, when Bragg peaks of metallic copper were observed. The end result was a composite electrode of an amorphous Li–V–O matrix with dispersed metallic copper. The essential point is the reversibility, with the disappearance of the metallic copper and the recrystallization of the initial $Cu_{2.33}V_4O_{11}$.

Two more examples belong to the class of intercalation materials: graphite as used for the negative electrode, and $LiNiO_2$ as a candidate for the positive electrode. 'Positive' and 'negative' electrodes are the preferred terms for secondary batteries instead of 'cathode' and 'anode', because anode and cathode reactions match only for discharge (interchange between the two electrodes occurs for the charge process). A comprehensive summary of structure reports on lithiated graphite can be found in Johnsen & Norby (2013). From the voltage plateau in cyclovoltammograms four distinct lithiated graphite phases have been postulated. However, only for two of them have complete structure models been reported and confirmed. The first is LiC_{12}, *P*6/*mmm* (space group No. 191), $a = 4.29$, $c = 7.03$ Å, with C on the 12*n* site with $x = 0.33$ and $z = 0.25$ and Li on the 1*a* site; the second is LiC_6, also *P*6/*mmm*, $a = 4.31$, $c = 3.70$ Å with C on the 6*k* site with $x = 0.33$ and Li again on the 1*a* site. According to the number of graphene layers that are needed for the smallest unit repeated by translational symmetry along the sixfold rotation axis, these structures are described as stage-II (LiC_{12}) and stage-I (LiC_6) compounds, like graphites intercalated with other alkaline elements. Note that in these phases the graphene layers are not shifted with respect to each other (*AA* sequence), in contrast to graphite (*AB* sequence). For a lower Li content, a much more complex structural behaviour was observed, including incommensurate Li distributions between the graphene layers, which were described as twisted bilayers (Senyshyn *et al.*, 2013). Higher-order reflections were observed for these phases and allowed indexing with a propagation vector (α, α, 0). Different structure models were discussed, but a complete description of the Li distribution is still lacking. Therefore, it is still an open question as to where the Li atoms in lithiated graphite are at low Li contents (below 1 Li per 12 C).

$LiNiO_2$ is considered to be a promising positive electrode material (Ohzuku *et al.*, 1993). However, it has some limitations, which are directly linked to the underlying structure. A high degree of cation disorder, *i.e.* Li on the Ni site and *vice versa*, hinders Li transport within the layers. Furthermore, Li and Ni exchange takes place rather easily, in contrast to $LiCoO_2$, because of a more favourable transport process through a tetrahedral interstitial site for Ni than for Co. In the cases of Li excess, $Li_{1+\delta}NiO_2$, or Ni excess, $(Li_{1-\delta}Ni_\delta)NiO_2$, some Ni^{2+} ions exist, which have a very similar ionic radius to that of Li^+. Therefore, it is nearly impossible to prepare stoichiometric $LiNiO_2$ with perfect separation of Li and Ni onto distinct layers. The best samples with respect to cation order are obtained from $NaNiO_2$ by successive Na $\rightarrow$ Li ion-exchange reactions. These drawbacks have prevented the commercial application of $LiNiO_2$, and more complex materials like $Li(Ni,Co,Al)O_2$ (NCA) and $Li(Ni,Co,Mn)O_2$ (NCM) are increasingly replacing $LiCoO_2$. Fig. 2.8.12 shows the structural changes in $LiNiO_2$ during the first charge and discharge. The detailed experimental conditions are the same as those described by Nikolowski *et al.* (2005) for $Li(Ni_{0.8}Co_{0.2})O_2$. One of the most characteristic features of the structural response to Li extraction and insertion is the pronounced change in the lattice parameters, shown by the changes in the *c*/*a* ratio for the rhombohedral structure. During Li extraction the *c* parameter increases, because there are fewer Li ions between (repulsive) O-atom layers. However, at lower Li contents, some of the O ions become oxidized, and the repulsion between the O-atom layers is weaker, resulting in shorter *c*-axis parameters. As a general rule, all layered oxides $LiMO_2$, with *M* = Mn, Co and/or Ni, become intrinsically unstable in the highly delithiated states beyond the maximum in the *c*/*a* ratio. Note that the as-prepared material has a very high degree of cation disorder (9.3% Ni on the Li site) and very poor capacity retention in the second cycle. The initial phase (*A*) gradually disappears and apparently transforms into a second phase (*B*) with a much lower degree of cation disorder (less than 3%). Note that this phase sequence does not necessarily reflect equilibrium conditions, but depends strongly on the chemical composition (Li or Ni excess), microstructure (size and strain) and the experimental conditions (charge rate, temperature, electrode formulation and more).

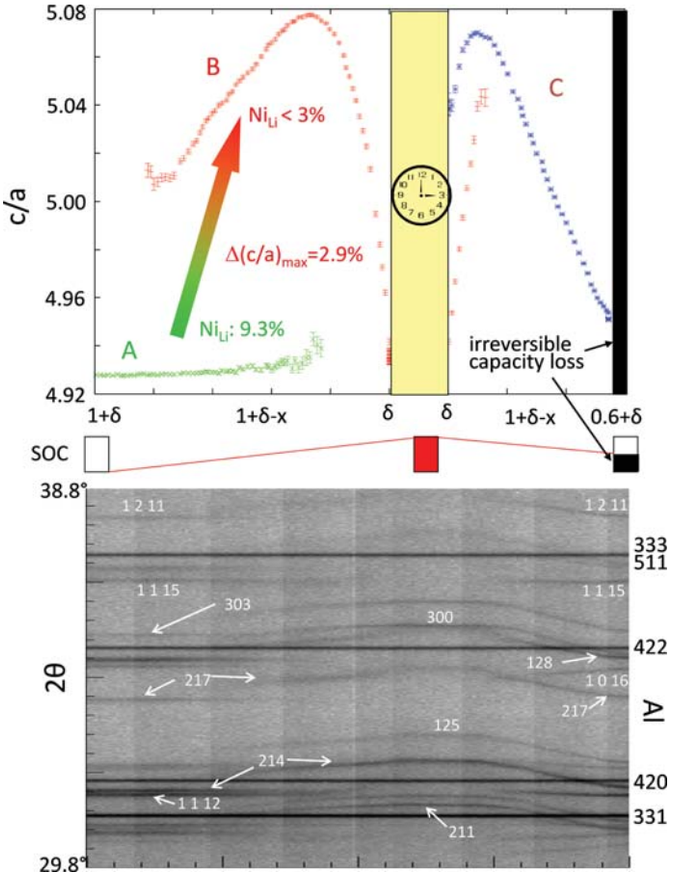

Figure 2.8.12
$Li_{1+\delta}NiO_2$ during charge and discharge. From about 210 complete diffraction patterns [a small section is shown below (λ = 0.499366 Å)], the structural response to Li extraction and insertion was monitored. In addition to changes in the unit-cell metric, the distribution of Li and Ni onto layers becomes more ordered during the first highly charged state. A pronounced capacity loss is observed during discharge after a holding time of 3 h in this overcharged state. A, B and C are three successively appearing phases. SOC = state of charge.

Such *in situ* studies are very important for elucidating the working mechanism and degradation processes for intercalation electrodes (Senyshyn *et al.*, 2012). Nevertheless, complementary methods are also essential for providing all the necessary information, especially about the surface near-interface region between the electrode and electrolyte, which has to be studied with surface-sensitive and local methods.

2.8.3.3. *Diffraction under a magnetic field*

2.8.3.3.1. *General remarks*

The majority of synchrotron and neutron experiments are currently limited to superconducting magnets with fields of 5–16 T. When higher fields are required there are essentially two possible solutions: pulsed resistive or steady-field resistive (or hybrid: resistive inner coil, superconducting outer coil) magnets. Pulsed fields are often used when signals are strong and the signal-to-noise ratio is good, whereas steady fields are primarily used for techniques with relatively long counting times and many data points. The relatively short pulse duration (from microseconds to milliseconds) along with the rather large sample volume required severely limit the use of pulsed magnetic fields in powder diffraction applications as well as more exotic methods of achieving high magnetic fields, *e.g.* magnetic flux compression or single-turn coils (Schneider-Muntau *et al.*, 2006). Furthermore,

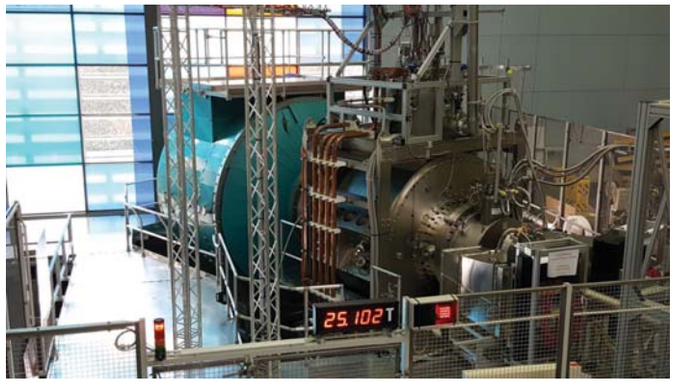

Figure 2.8.13
The High Magnetic Field Facility for Neutron Scattering at the Helmholtz-Zentrum Berlin has two main components: the High Field Magnet (HFM) and the Extreme Environment Diffractometer (EXED). Courtesy of Dr O. Prokhnenko.

because of the large stresses, the lifetime of a resistive/pulsed magnet is finite: pulsed magnets have typical lifetimes of 500 shots at 95% of the design field, and their lifetimes are virtually independent of pulse duration.

At present, the maximum field for technical superconductors is 23 T and modern developments in superconductor design along with robust magnet manufacturing techniques have made possible high-flux-density magnets for neutron scattering studies up to 16 T. For resistive magnets, there are in principle no limitations to the generation of the highest continuous fields apart from economics, as approximately 1 MW of electric power is consumed per 1 T field strength. Therefore, in order to reduce the running costs (*i.e.* the required power per unit magnetic field), hybrid magnets are becoming increasingly popular. In this context we mention the joint developments between the National High Magnetic Field Laboratory (Tallahassee, FL, USA), the Spallation Neutron Source (Oak Ridge, TN, USA) and Helmholtz-Zentrum Berlin (Germany) in the development of high-steady-field (25 T with a 4 MW resistive insert, 30 T with an 8 MW resistive insert) hybrid magnets for neutron scattering (Bird *et al.*, 2009). A high-field magnet has been installed and is in routine user operation (Fig. 2.8.13) at the Extreme Environment Diffractometer (HFM-EXED) of Helmholtz-Zentrum Berlin (Prokhnenko *et al.*, 2015).

On the other hand, it is quite simple to produce magnetic flux density uniformity or homogeneity over the required sample volume down to the p.p.m. level with a solenoid magnet. However, the majority take the form of split-pair solenoids. With this setup, the access to the sample environment (along the magnetic axis) can be orthogonal to the beam-access plane. The split-coil setup is the most popular in neutron scattering, but the geometry constraints imposed by the neutron aperture make the creation of very uniform flux density much more difficult. In general, for a typical neutron-scattering sample volume of 1 cm^3, the magnetic field homogeneity is normally limited to the range 0.1 to 5%. As the available current density for a given conductor decreases with increasing flux density, the flux density seen by the superconductor inside the magnet windings is greater than the 'nominal' central value. This is particularly the case for split-pair magnets, where the ratio of the two can be large, *e.g.* for a central value of 9 T, a ratio of 1.6 gives a maximum flux density of 14.3 T (Brown, 2010).

As already pointed out, diffraction studies under a magnetic field are almost always performed with neutrons. However,

references